ACS OMEGA

http://pubs.acs.org/journal/acsodf

Article

Facile and Green Engineering Approach for Enhanced Corrosion Resistance of Ni−Cr−Al_2O_3 Thermal Spray Coatings

Harpreet Singh Arora,*,# Gopinath Perumal,# Manjeet Rani, and Harpreet S Grewal

Cite This: *ACS Omega* 2020, 5, 24558−24566

Read Online

ACCESS | Metrics & More | Article Recommendations | Supporting Information

ABSTRACT: Thermal spray coatings (TSCs) are widely utilized for limiting degradation of structural components. However, the performance of TSCs is significantly impaired by its inherent non-homogeneous microstructure, comprising of splat boundaries, porosities, secondary phase-formation, and elemental segregation. Herein, we report a simplistic approach for significantly enhancing the corrosion resistance of TSCs. Ni−Cr−5Al_2O_3 coatings were deposited on stainless steel using high-velocity oxy-fuel technique. The microstructure of as-sprayed coating showed significant inhomogeneities in the form of isolated splats and elemental segregation. The microstructure of developed coatings was modified using a novel processing technique, known as stationary friction processing (SFP). The SFP treatment resulted in complete refinement of coating microstructure with elimination of splat boundaries and pores along with elemental homogenization. The corrosion behavior of as-sprayed and SFP treated coating was evaluated in 3.5% NaCl solution using potentiodynamic polarization and electrochemical impedance spectroscopy. The SFP treatment reduced the corrosion rate of as-sprayed coating by an order of magnitude. Long-time immersion studies showed continuously decreasing impedance of the as-sprayed coating due to the penetration of the electrolyte along the splat boundaries. In contrast, impedance for the SFP treated coating increased with the immersion time due to the removal of all microstructural defects.

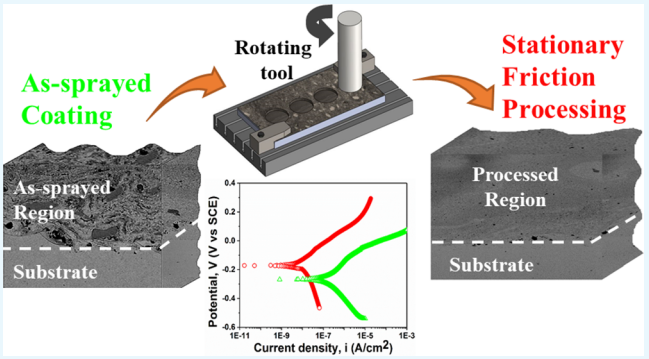

1. INTRODUCTION

Thermal spray coatings are widely used for limiting material degradation by corrosion,[1−6] erosion,[7,8] and wear.[9,10] Thermal spray techniques are categorized based on the energy source utilized to develop the coatings from the feedstock powder.[11] Among all the thermal spray processes, high-velocity oxy-fuel process (HVOF) is known to have one of the largest application base. This is due to the low porosity level and good adhesion of the coating with the substrate. On the downside, the non-homogeneous lamellar microstructure of thermal spray coatings is a huge concern. The inter-splat boundaries, elemental segregation zones, and pores are the defect sites with localized stress concentration, leading to premature coating failure during service.[12] Further, these defect sites serve as pathways for the electrolyte penetration into the interior, resulting in accelerated corrosion.[12] It is evident that the performance and durability of thermal spray coatings can be substantially improved by eliminating these defect sites through microstructural refinement.

Typically, the as-sprayed thermal spray coatings are treated with chemicals and organic sealants for enhancing their degradation resistance. Epoxy-based sealants are widely used for filling up the pores and splat boundaries in the as-sprayed microstructure.[13−15] However, the utilization of epoxy resins causes severe environmental issues due to poor recyclability. Further, the disposal of epoxy resins is also difficult due to their stable network structures and generally results in byproducts containing toxic molecules, which are difficult to be separated and reutilized.[16,17] In addition, various post-processing treatments are also utilized for enhancing the corrosion resistance of thermal spray coatings by eliminating its inherent defects. These include furnace heating,[18−20] microwave sintering,[21] laser treatment,[22−24] plasma treatment,[25] and thermo-mechanical techniques, such as friction stir processing (FSP).[26,27] High-temperature furnace annealing has problems associated with oxidation, while low-temperature heating for longer times can deteriorate the mechanical properties of the substrate through grain growth.[18] Laser and plasma heat treatments require highly specialized equipment with huge capital investments, which limits their practical applications. In addition, previous studies also report on significant coating dilution during laser, plasma, or microwave treatments through mass transport from the

Received: June 24, 2020
Accepted: September 2, 2020
Published: September 16, 2020

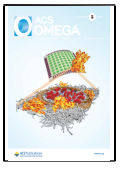

https://dx.doi.org/10.1021/acsomega.0c03053
ACS Omega 2020, 5, 24558−24566

substrate.[28,29] Significant coating dilution can deteriorate its performance through compositional changes and thus must be prevented. In contrast, friction stir processing is a versatile technique, which has been largely utilized for microstructural refinement in both bulk materials[30,31] as well as surface coatings.[26,32] The combined thermal and strain field experienced by the specimen during FSP significantly reduces the processing time while enhancing the efficiency. However, the influence of friction stir processing is typically limited to a small depth underneath the surface. Thus, it is unlikely for friction stir processing to achieve through microstructural refinement of the coating resulting in a weaker coating-substrate interface. Therefore, it is imperative to develop an efficient environment friendly processing technique for minimizing microstructural inhomogeneities across the entire coating depth.

In the current work, we have utilized a novel processing technique, known as stationary friction processing (SFP) for the post-processing of Ni−Cr−Al_2O_3 coatings. Ni−Cr−Al_2O_3 composition was used in this study owing to its superior corrosion resistance. Ni-53 at % Cr forms a near eutectic composition with complete miscibility in both liquid and solid states. Further, chromium (Cr) was added to Ni−Al_2O_3 composition for enhancing the corrosion resistance of the alloy as well as wettability of Ni with Al_2O_3. The SFP is a highly simplistic technique based on the principles of green engineering. The process is completely environmental friendly as no chemicals or reagents are utilized. Further, the process does not produce any harmful byproducts. In addition, the process is highly energy efficient due to its inherent ability to process the material in a few minutes compared to several hours for currently utilized furnace annealing for microstructural refinement. The SFP treatment significantly enhanced the corrosion behavior of the coating, which was attributed to complete microstructural rejuvenation up to the coating-substrate interface. This is the first detailed report on the utilization of this novel processing technique for significantly enhancing the material's corrosion performance. The study establishes stationary friction processing to be a highly versatile toolbox for engineering superior corrosion performance in a wide range of materials and coatings.

2. RESULTS AND DISCUSSION

2.1. Microstructure. SEM images showing the microstructure of as-sprayed coating at the top surface are shown in Figure 1a,b while cross section images are shown in Figure 1c,d. The as-sprayed coating reveals a splat-like morphology, typical of thermal-spray processes. Regions with different contrasts highlight its non-homogeneous microstructure with element/phase segregation. The thickness of as-sprayed coating was estimated to be nearly 250 μm. The density of as-sprayed coating was measured to be 6.65 gm/cm^3, while coating porosity was estimated to be nearly 2.5 ± 0.5% using ImageJ software. Figure 1e−j shows EDAX analysis of the as-sprayed coating.

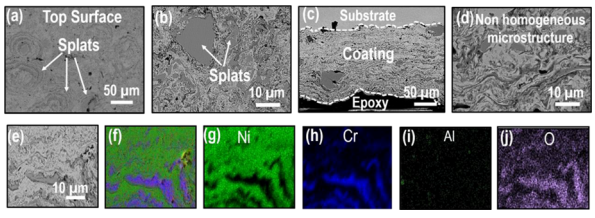

Figure 1. (a) SEM image showing microstructure of as-sprayed Ni−Cr−5Al_2O_3 coating at the top surface, (b) magnified image of region marked in (a), (c) SEM images showing microstructure of as-sprayed Ni−Cr−5Al_2O_3 coating along the cross section, (d) magnified image of coating shown in (c), and (e− j) EDAX analysis of as-sprayed coating showing non-uniform element distribution.

The elemental distribution in the as-sprayed coating is highly non-homogeneous with the formation of isolated Ni and Cr splats/islands, the primary constituents of the coating. Further, EDAX mapping suggests formation of Ni and Cr oxides, likely due to high-operating temperature during coating deposition. A schematic representation of microstructure refinement using FSP and SFP techniques are shown in Figure 2. While FSP is a well-known technique for microstructural refinement, SFP is a novel processing technique utilized in this study. SFP resulted in complete refinement of non-homogeneous as-sprayed microstructure up to the coating-substrate interface while the depth of microstructural refinement is only partial for FSP. Figure 3 shows the SEM images following FSP (Figure 3 a−d) and SFP (Figure 3e−h) treated coatings. It is evident that the coating microstructure got refined after FSP; however, some splat boundaries still exists on the top surface (Figure 3b). In contrast, the SFP sample reveals a completely refined microstructure without any splats and splat boundaries (Figure 3f). Further,

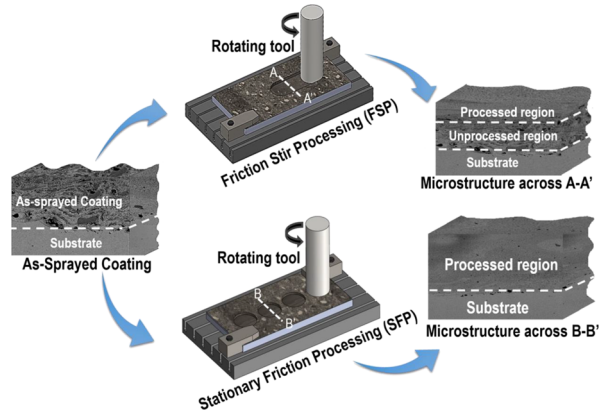

Figure 2. Schematic representation of the processing techniques used in the current study for tailoring the properties of as-sprayed coating i.e., friction stir processing (FSP) and stationary friction processing (SFP). The microstructure across lines A-A′ and B-B′ are shown alongside.

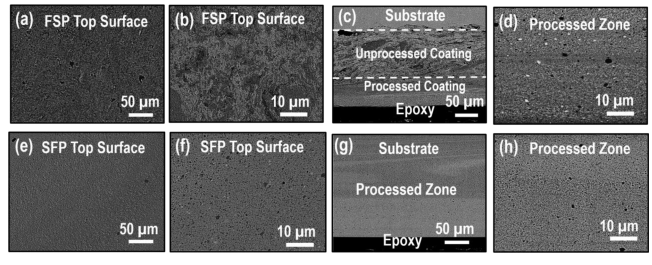

Figure 3. (a) SEM image showing microstructure at the top surface of FSP treated Ni−Cr−5Al_2O_3 coating, (b) magnified image of coating shown in (a), (c) SEM image showing microstructure across the cross section of FSP treated Ni−Cr−5Al_2O_3 coating, (d) magnified image of coating shown in (c), (e) SEM image showing microstructure at the top surface of SFP treated Ni−Cr−5Al_2O_3 coating, (f) magnified image of coating shown in (e), (g) SEM image showing microstructure across the cross section of SFP treated Ni−Cr−5Al_2O_3 coating, and (h) magnified image of coating shown in (g).

https://dx.doi.org/10.1021/acsomega.0c03053
ACS Omega 2020, 5, 24558−24566

FSP-processed sample shows microstructure refinement up to nearly 50 μm depth only, as evident from the cross section SEM image shown in Figure 3c. The region below 50 μm depth remained unaltered, which is evident by the presence of the splat-type morphology, similar to the as-sprayed coating. In contrast, SFP resulted in through-thickness refinement of the coating and coating-substrate interface is nearly indiscernible (Figure 3g). The magnified image of SFP and FSP treated samples are shown in Figure 3d and h, respectively. The EDAX mapping of SFP treated coating, shown in Figure S1, indicates complete homogenization of all constituent elements. The coating thickness after processing got reduced to nearly 150 μm due to the removal of some material by the plunge action of the processing tool. The porosity for both FSP and SFP was negligible and cannot be determined by image analysis. The experimental density of FSP and SFP treated samples was found to be 6.83 and 7.41 g/cm^3,respectively, while the theoretical density was calculated to be 7.57 g/cm^3. Thus, the experimental density for the SFP treated sample is nearly the same as theoretical density, which also supports complete elimination of pores and other defects from the coating. The XRD analysis (Figure 4) indicates large fraction of chromium oxide in the bulk

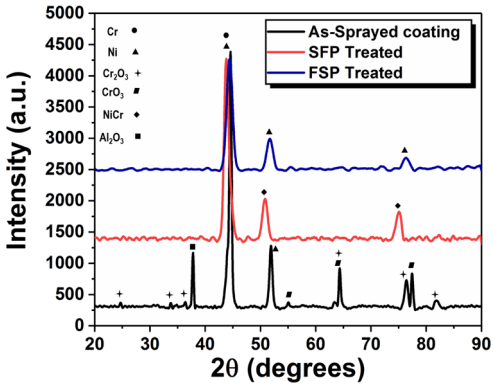

Figure 4. XRD analysis of the as-sprayed coating, SFP, and FSP treated coating.

of the as-sprayed coating while SFP treated coating was primarily comprised of solid solution. The formation of chromium oxide in the as-sprayed coating is also shown by the EDAX analysis (Figure 2). The crystallite grain size for the as-sprayed, SFP treated coating, and FSP treated coating was calculated from the XRD analysis using the Scherrer equation (eq 1)[33]

$$m = \frac{k\lambda}{D\cos\theta} \quad (1)$$

where m is the full width at half maximum (FWHM, obtained from XRD data), D is the crystal grain size, λ is the wavelength, θ is the diffraction angle, and k is the Scherrer constant having a value in the range of 062−2.08. The most commonly used value of k is taken as 0.89. The crystallite size for the as-sprayed coating, SFP treated, and FSP treated samples was found to be 16.66, 8.44, and 7.47 nm, respectively. Thus, the severe plastic deformation of the coating resulted in reduction in the crystallite grain size. Finer crystallite grain size is favored when the dislocation motion is impeded, leading to rearrangement of dislocations into cell boundaries. The severe plastic deformation during SFP and FSP likely increases the dislocation density while formation of Ni−Cr solid solution impedes their movement, resulting in a finer crystallite grain size. Previous studies have also shown reduction in the crystallite grain size after severe plastic deformation.[34] Thus, SFP resulted in complete rejuvenation of the coating through removal of all as-sprayed defects, uniform elemental distribution, dissolution of metal oxides, as well as reduction in crystallite grain size. It is evident that SFP is more effective than FSP in achieving complete microstructural refinement. This is likely attributed to larger interaction time between the processing tool and the workpiece during SFP compared to FSP. The high strain and temperature field during SFP resulted in fragmentation of splats and splat boundaries, elimination of porosities, and accelerated diffusion kinetics of constituent elements. The longer processing time at a localized location during SFP favors the deformation to spread down to the coating-substrate interface making the coating homogeneous up to the interface.

2.2. Potentiodynamic Polarization. Potentiodynamic polarization behavior of as-sprayed coating, both the processed coating samples and stainless steel substrate in 3.5% NaCl solution are shown in Figure 5. The as-sprayed coating, FSP

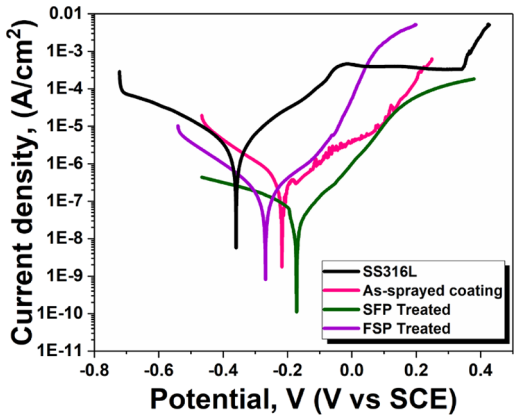

Figure 5. Potentiodynamic polarization curves for the stainless steel substrate, as-sprayed coating, FSP, and SFP treated Ni−Cr−5Al_2O_3 coatings in 3.5% NaCl solution.

processed sample, and stainless steel substrate showed an active behavior indicated by a rapid increase in the current density while SFP treated coating showed an active−passive behavior wherein an initial surge in corrosion current is followed by a potential increase at nearly constant current density. Different corrosion parameters, including corrosion current (I_{corr}), corrosion potential (E_{corr}), and corrosion rate (mils per year, mpy) are extracted using Tafel fitting and are shown in Table 1. Corrosion current, which is an indicator of material's corrosion rate, was found to be nearly 0.4 μA/cm^2 for the as-sprayed coating compared to nearly 7.71 μA/cm^2 for the stainless steel substrate. The corrosion current for both the processed samples

Table 1. Corrosion Parameters Obtained from Potentiodynamic Polarization Measurements for as-Sprayed, FSP Treated, and SFP Treated Ni−Cr−5Al_2O_3 Coatings in 3.5% NaCl Solution

sample	I_{corr} (μA/cm^2)	E_{corr} (mV)	CPY(mpy)
as-sprayed coating	0.4	−217	0.131
SFP coating	0.08	−162	0.026
FSP coating	0.23	−268	0.124
substrate-SS316L	7.71	−359	3.476

https://dx.doi.org/10.1021/acsomega.0c03053
ACS Omega 2020, 5, 24558−24566

were significantly lower with 0.23 μA/cm^2 for the FSP specimen while it was nearly 0.08 μA/cm^2 for the SFP specimen. The corrosion current and thus corrosion rate for SFP specimen is nearly five times lower compared to as-sprayed coating. Further, E_{corr} for the SFP specimen was found to be nobler compared to FSP and the as-sprayed coating specimen. Higher corrosion potential of the SFP specimen signifies its lower thermodynamic tendency for corrosion. Significantly higher corrosion resistance of the SFP coating specimen is attributed to complete homogenization of the coating microstructure with removal of all coating defects. The interface between different splats is highly prone to localized corrosion due to composition gradients across the splats and/or thermal stresses developed via solidification during coating synthesis. Removal of all such corrosion prone sites likely resulted in high corrosion resistance of the SFP treated coating. Further, dissolution of metal oxides in the coating following processing also contributes to their improved corrosion resistance. The measured current densities can be utilized to quantitatively estimate the coating porosity using eq 2[35]

$$P = \frac{i_c}{i_s} \times 100\% \quad (2)$$

where P is the connected porosity of the coating, i_c is the corrosion current density of the coated substrate, and i_s is the corrosion current density of the substrate in the same electrolyte. The estimated coating porosity using the above relation was nearly 5%, which is slightly higher than the value determined through microstructural analysis (~3% max.). This may be due to some small micropores, which remain unidentified/unaccounted during microstructural analysis. The above relation estimates nearly 1% porosity for the SFP specimen, 5 times lower than the as-sprayed coating. SEM images at the top surface of corroded as-sprayed coating showed huge pit formation, primarily at splat boundaries (Figure S2 a,b). In contrast, corrosion pits are significantly smaller for FSP specimen (Figure S2c,d). The surface of the SFP specimen showed negligible pit formation (Figure S2e,f), supporting its high corrosion resistance.

The SEM images of cross section samples subjected to corrosion testing are shown in Figure 6. The magnified region close to region 1 (Figure 6a,b) shows pit formation at splat boundaries while region 2 is the interface between coating and the substrate. The interface of as-sprayed coating is severely pitted due to the formation of strong galvanic cells (Figure 6c). Pitting within the processed zone for the FSP specimen (marked 1 in Figure 6d,e) is minimal; however, the coating-substrate interface (region 2 in Figure 6f) shows fine corrosion pits. This is attributed to non-homogeneous as-sprayed microstructure at the coating-substrate interface for the FSP specimen (Figure 3c). In contrast, corrosion pits are not observed anywhere for the SFP specimen (Figure 6g–i), which is attributed to its through-thickness refinement, complete elemental homogenization, and defect-free microstructure. The surface chemistry, probed using XPS, was found to be nearly similar for all the samples (Figure S3a). The atomic percentage of oxides of Al, Cr, and Ni indicates that the passive layer is rich in aluminum oxide, followed by chromium oxide and nickel oxide (Figure S3b). Further, the passive layer formed on the SFP sample has higher chromium oxide compared to the as-sprayed and FSP specimen. This is likely attributed to dissolution of chromium oxide during SFP that resulted in enhanced elemental diffusion. Higher Cr fraction in the passive layer might have also contributed toward the superior corrosion performance of the SFP specimen.

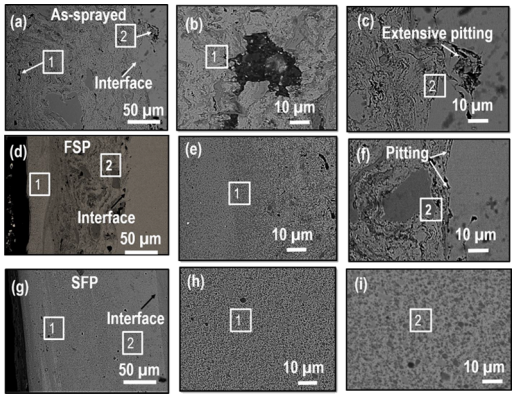

Figure 6. Cross section SEM images after potentiodynamic polarization testing (a–c) as-sprayed Ni–Cr–5Al_2O_3 coating, (d–f) FSP treated Ni–Cr–5Al_2O_3 coating, and (g–i) SFP treated Ni–Cr–5Al_2O_3 coating.

2.3. EIS Measurements for Long-Time Immersion. Impedance spectra are widely used to evaluate the coating effectiveness in restricting corrosion over long exposure periods.[1,2,15,36−38] In the current study, the impedance characteristics of the as-sprayed and SFP coatings were obtained as a function of time over a period of 168 h. Figure 7 shows the impedance data for the as-sprayed coating. The OCP variation as a function of immersion time is shown in Figure 7a. It is seen that the potential of the as-sprayed coating reduces for each successive day, indicating its higher thermodynamic tendency for corrosion with time. The Nyquist and Bode plots for the as-sprayed coating for different immersion times are shown in Figure 7b–d. The impedance spectra decreased continuously with the immersion time, indicating deterioration in the as-sprayed coating's corrosion resistance over a period of time. Figure 7c shows the Bode phase plot for the as-sprayed coating at different immersion times. The phase plot showed a single inflexion for the first 24 h while the curve has two inflexions for 24–168 h period. The presence of two inflexions in the curve indicates two relaxation processes or the time constants. High frequency time constant (at ~100 Hz frequency) corresponds to the dielectric properties of the coating while low frequency time constant (at ~1 Hz frequency) represents the coating defects including porosities.[36] Thus, impedance at the high frequency represents the performance of the coating in the electrolyte while low-frequency impedance is related to the corrosion at the substrate/solution interface. Therefore, the low frequency part of the Bode plot can be used to as an indicator of the coating performance. It is seen that for the as-sprayed coating, the low frequency impedance decreases with the immersion time which also signifies the poor corrosion performance of the as-sprayed coating for longer immersion times (Figure 7d).

The impedance results for the SFP specimen are shown in Figure 8. The variation of OCP as a function of immersion time is shown in Figure 8a. In contrast to the as-sprayed coating, SFP showed a systematic increase in the potential with successive immersion days. Nobler potential signifies an increase in corrosion resistance with time. The Nyquist plot for the SFP specimen at different immersion times is shown in Figure 8b. The impedance spectra increased continuously with each successive day and shows only one mid-frequency capacitive loop, corresponding to inflexion in the Bode phase plot at

https://dx.doi.org/10.1021/acsomega.0c03053
ACS Omega 2020, 5, 24558−24566

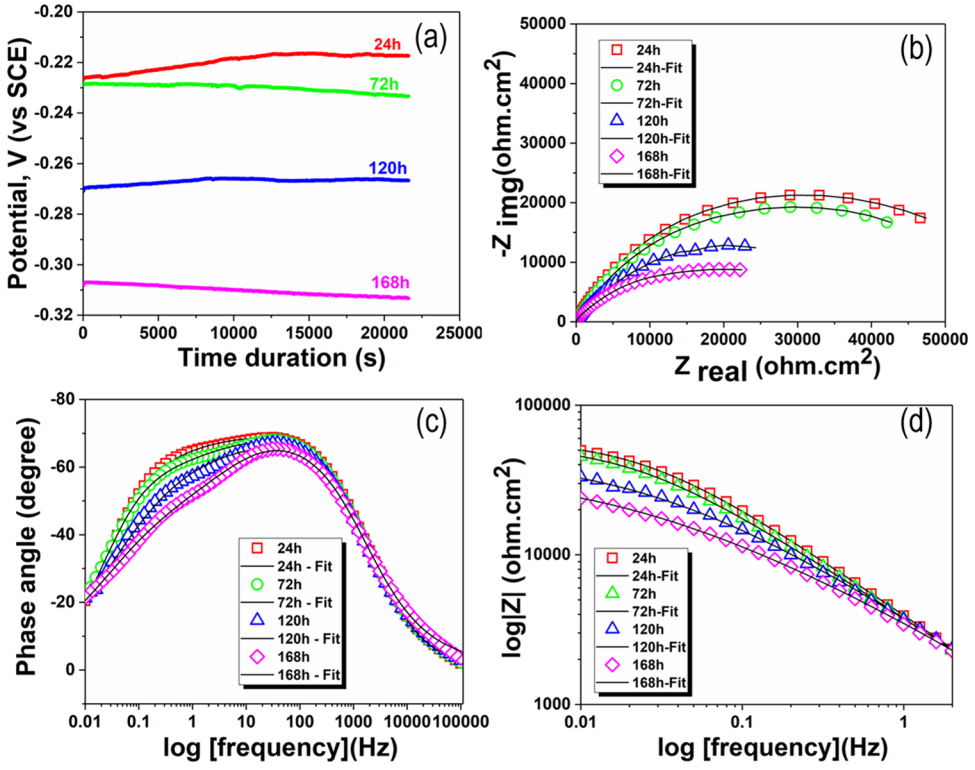

Figure 7. (a) OCP variation, (b) Nyquist plot, (c) Bode phase plot, and (d) low frequency impedance plot for as-received Ni−Cr−5Al_2O_3 coating for a period of 168 h.

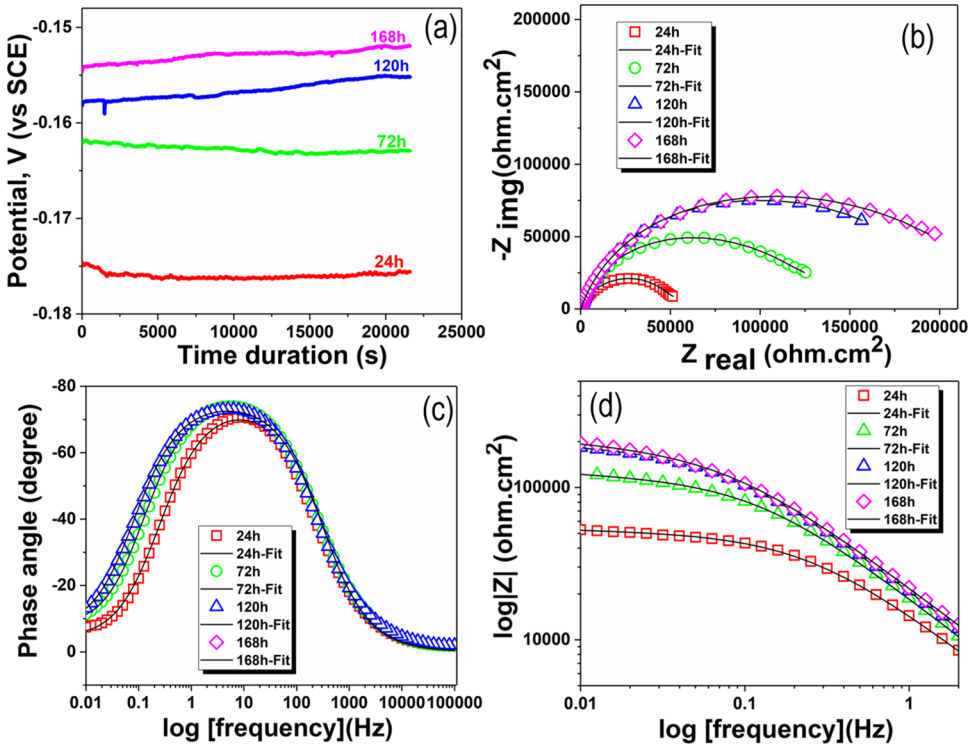

Figure 8. (a) OCP variation, (b) Nyquist plot, (c) Bode phase plot, and (d) low frequency impedance plot for SFP treated Ni−Cr−5Al_2O_3 coating for a period of 168 h.

around 10 Hz frequency (Figure 8c). The increase in peak height indicates better capacitive behavior at longer immersion times for the SFP specimen. Further, the low frequency region of the Bode phase plot shows an increase in the impedance with the immersion time (Figure 8d). This indicates high corrosion resistance of the SFP specimen, likely due to the formation of the stable passive layer with the immersion time. The schematic of coating-electrolyte interaction and equivalent electrical circuits

https://dx.doi.org/10.1021/acsomega.0c03053
ACS Omega 2020, 5, 24558−24566

(EEC) for the as-sprayed coating are shown in Figure 9a,b. A single RC circuit is used for the initial period of 24 h,

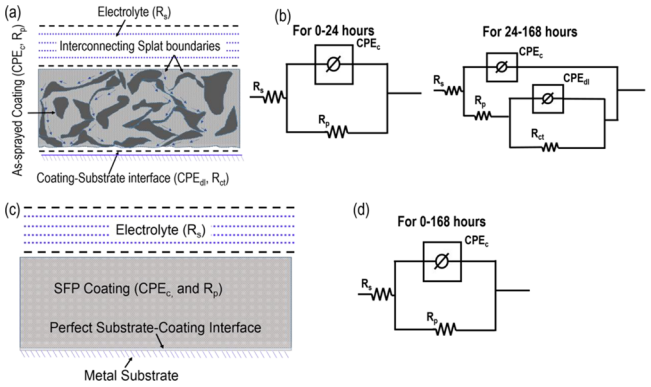

Figure 9. (a) Schematic of coating-electrolyte interaction, (b) electrical equivalent circuits (EEC) for the as-sprayed coating, (c) schematic of coating-electrolyte interaction, and (d) electrical equivalent circuit (EEC) for SFP treated coating.

corresponding to the single time constant while a double RC circuit is used for 24−168 h period. Here, R_s is the solution resistance, CPE_{dl} and R_{ct} describe the electrical charge transfer at the substrate-coating interface and denote the constant-phase element and resistance of the steel substrate, respectively. In series with CPE_{dl} and R_{ct}, R_p is the pore electrical resistance of the ionic current through the pores and CPE_c represents the constant phase element for the coating. CPE, representing a leaky or a non-ideal capacitor, is considered here instead of a pure capacitor to account for surface heterogeneities. Typically, the true surface area of the exposed specimen is greater than its geometric surface area owing to roughness. With the exposure time, the difference between true and geometric area further increases due to corrosion. In addition, surface defects, including grain boundaries, dislocations, and impurities enhance the surface inhomogeneities. The constant phase element accounts for these interfacial characteristics rather than a pure capacitor. Impedance for CPE is given by the following eq 3 below[36]

$$Z_{CPE} = 1/[Y_0(j\omega)^n] \quad (3)$$

where Y_o is the admittance magnitude of CPE and n is the exponential term. For pure capacitor, $n = 1$. For the equivalent circuit shown in Figure 8b, the real and imaginary components of the impedance are given by Z' and Z'', eqs 4 and 5, respectively[39]

$$Z' = R_s + \frac{R_p + R_{ct} + \omega^2(CPE_{dl}R_{ct})^2R_p}{(1 - \omega^2R_{ct}CPE_{dl}R_pCPE_c)^2 + \omega^2(R_{ct}CPE_{dl} + R_{ct}CPE_{dl} + R_pCPE_c)^2} \quad (4)$$

$$Z'' = -\frac{\omega[R_{ct}^2CPE_{dl}(1 + \omega^2R_p^2CPE_{dl}CPE_c) + C_c(R_p + R_{ct})^2]}{(1 - \omega^2R_{ct}CPE_{dl}R_pCPE_c)^2 + \omega^2(R_{ct}CPE_{dl} + R_{ct}CPE_{dl} + R_pCPE_c)^2} \quad (5)$$

The schematic of coating-electrolyte interaction and equivalent electrical circuit for the SFP specimen are shown in Figure 9(c) and d, respectively. Interestingly, the EEC for SFP is relatively simpler and is comprised of only one RC circuit where R_s, CPE_c, and R_p have usual meanings as above. The values of different fitting parameters for the as-sprayed and SFP treated coatings are given in Tables 2 and 3, respectively.

Table 3. EIS Fitting Parameters for the SFP Treated Coating

time duration	R_p (k ohm cm^2)	CPEc (μ S s^n cm^{-2})	n_1
24 h	73.304	13.48	0.839
72 h	162.448	10.75	0.855
120 h	196.504	9.94	0.842
168 h	199.068	9.61	0.835

The variation of coating capacitance and the pore resistance as a function of immersion time was obtained for as-sprayed and SFP specimen and is shown in Figure 10. As-sprayed specimen showed a three-stage variation in capacitance, comprising of an initial increase at lower immersion time followed by nearly steady state during the intermediate time duration and rapid increase in the capacitance toward the later stages (Figure 10a). An initial rise in capacitance is likely due to rapid penetration of the electrolyte into the as-sprayed microstructure, which reduces the dielectric properties of the coating, and hence results in an increase in the coating capacitance. The inherent defects in the as-sprayed coating, including splat boundaries and pores provide an easy path for the electrolyte uptake, resulting in rapid impregnation. Once the pores and splat boundaries get saturated with the electrolyte, the capacitance saturates resulting in nearly steady-state capacitance. For the current study, the saturation of the coating with electrolyte occurred after nearly 60th h. The coating capacitance remained nearly steady for the next 50 h followed by a rapid increase in the capacitance at later stages. A sharp rise in the capacitance indicates penetration of the electrolyte through the entire coating thickness, reaching the coating-substrate interface. In addition, a rapid increase in coating capacitance in the third stage also signifies concomitant electrochemical activity beneath the coating resulting in coating delamination. The under-film corrosion can result in adhesion loss, detachment, and failure of the coating.[40] As proposed by Mišković-stanković et al.,[41] the mechanism of coating failure involves two-steps water uptake into the coating followed by water and ion penetration along with opening of new macro-pores. The water uptake results in the initial increase of the capacitance followed by steady state at a later stage. The penetration of water and ions with opening of new macro-pores results in significant capacitance increase at the third stage. In contrast, there is a slight decrease in the coating capacitance as a function of immersion time for the SFP specimen, indicating absence of electrolyte penetration and superior adhesion with the substrate. In concurrence with increasing capacitance, pore resistance decreased with the immersion time for the as-sprayed

Table 2. EIS Fitting Parameters for the As-Sprayed Coating

time duration	R_p (k ohm cm^2)	R_{ct} (k ohm cm^2)	CPE_c (μ S s^n cm^{-2})	n_1	CPE_{dl} (μ S s^n cm^{-2})	n_2
24 h	60.83		60.30	0.772		
72 h	56.5	0.597	68.47	0.782	186	0.89
120 h	41.13	0.925	77.85	0.747	136.3	0.90
168 h	31.03	2.047	100.5	0.730	109.7	0.85

https://dx.doi.org/10.1021/acsomega.0c03053
ACS Omega 2020, 5, 24558−24566

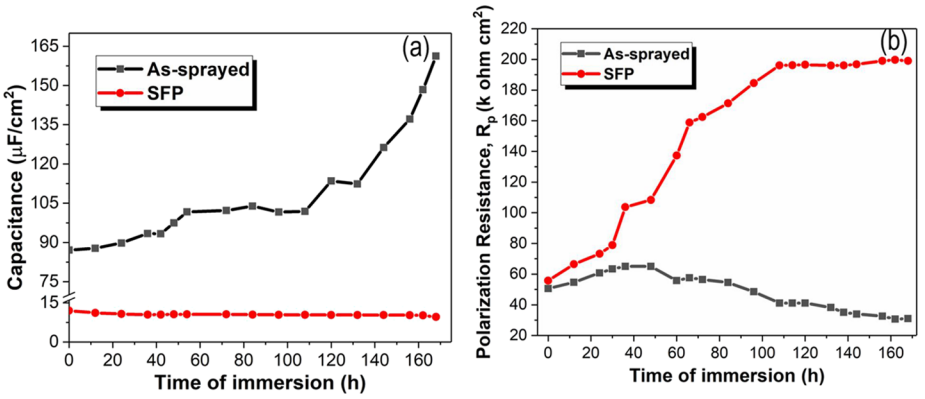

Figure 10. Variation of (a) coating capacitance and (b) coating resistance as a function of immersion time for the as-sprayed as well as SFP treated Ni−Cr−5Al_2O_3 coating.

coating (Figure 10b). An initial decrease in the pore resistance up to 60th h is followed by a steady state up to 100th h and a continuous decrease thereafter. The electrolyte penetration into the coating increases the ionic conductivity concurrent with decrease in the pore resistance. In contrast, the pore resistance for SFP was found to continuously increase with the immersion time, indicating high resistance to electrolyte penetration in a densified and defect-free microstructure. This is the consequence of through-thickness microstructure refinement for the SFP specimen, as discussed above. Thus, SFP provides a unique pathway to significantly enhance the degradation resistance of TSCs through complete microstructural transformation.

3. CONCLUSIONS

The microstructure of as-sprayed Ni−Cr−5Al_2O_3 coatings was modified using a novel processing technique known as stationary friction processing (SFP). The corrosion rate for the SFP treated coating sample was found to be nearly 5 times lower compared to as-sprayed coating. SEM analysis showed localized corrosion at the splat boundaries of the as-sprayed coating. Electrochemical impedance studies showed a decrease in the coating resistance over time for the as-sprayed coating concurrent with the increase in coating capacitance. This is attributed to penetration of the electrolyte, likely through pores and splat boundaries, which served as diffusion channels. In contrast, the SFP treated sample showed an increase in pore resistance with immersion time without any evidence of liquid penetration through the coating. The remarkable improvement in the corrosion performance of coating after SFP treatment is attributed to complete microstructure homogenization along with removal of all the defect sites. The current study demonstrates that SFP could be a unique pathway for developing superior corrosion resistant surfaces.

4. MATERIALS AND METHODS

4.1. Processing Details. Ni−Cr−5 wt % Al_2O_3 coatings were deposited on stainless steel, SS316L, substrate. The deposition technique used for the current study was high velocity oxy fuel (HVOF; Metallizing Equipment Co. Pvt. Ltd.; model HIPOJET-2700) which was performed at Metallizing Equipment, India. Table S1 gives the powder size and deposition parameters used in the current study. For ensuring good adhesion of the coating, the substrate was shot peened prior to the deposition. The coated samples were processed using two different techniques: (1) friction stir processing (FSP), wherein a pinless cylindrical tool made of tungsten carbide was traversed over the surface of the coating. The tool diameter of 12 mm, rotational speed of 388 rpm, plunge depth of 0.25 mm, and transverse speed of 20 mm/min were used. These parameters were optimized during the trial runs, (2) stationary friction processing (SFP), this is a novel processing technique wherein the tool was rotated at a particular location of the workpiece for a period of 5 min. The processing conditions used in this case were similar to FSP with a difference that there was no transverse motion of the tool. Both FSP and SFP were performed on a universal milling machine (Kaizen; model XW6032A).

4.2. Microstructural Characterization. The as-sprayed and processed coating samples were sectioned in the dimensions of 10 mm × 10 mm × 3 mm for microstructural characterization. All samples were ground to 3000 grit paper and then polished to mirror finish, followed by ultrasonically cleaned in acetone, washed in distilled water, and dried in warm air. Microstructure of as-sprayed and processed coatings was analyzed using scanning electron microscope (model, Nova Nano FE-SEM 450; FEI, Hillsboro, Oregon, USA) equipped with energy dispersive spectroscopy (Bruker, Billerica, Massachusetts, USA) and X-ray diffraction (D8 Discover; Bruker AXS, Karlsruhe, Germany). The thin oxide film formed on all samples was characterized by x-ray photoelectron spectroscopy (XPS). XPS spectra of Cr, Al, Ni, and O were recorded on the surface of all the samples using monochromatic Al Kα X-ray source (1.486 keV, Scienta Omicron Nanotechnology). The obtained spectra were de-convoluted and atomic percentages were calculated using Casa XPS (V2.3) software.

4.3. Corrosion Studies. Corrosion behavior of as-sprayed and processed coating samples was investigated by open circuit potential (OCP), potentiodynamic polarization and electrochemical impedance spectroscopy (EIS) using Gamry Interface 1000-E electrochemical setup. The cross section of all samples was also subjected to corrosion testing to evaluate the corrosion behavior across the sample depth. A standard three-electrode cell configuration was used with saturated calomel electrode (SCE) as a reference, high-density graphite rod as a counter, and sample as the working electrode. NaCl solution (3.5%) was used as an electrolyte. Potentiodynamic polarization was done in the voltage range of −0.25 V vs E_{OCP} to 0.45 V vs E_{OCP} with a scan rate of 0.166 mV/s. EIS measurements were obtained at E_{OCP} over a frequency range of 0.01 Hz to 100 kHz with a set AC voltage amplitude of 10 mV over a period of 168 h. Equivalent electrical circuit (EEC) was modeled and obtained data was fitted by simplex algorithm using Gamry E-chem analyst 7.05. All the experiments were done three times to ensure the

https://dx.doi.org/10.1021/acsomega.0c03053
ACS Omega 2020, 5, 24558−24566

repeatability. The surface of corroded samples was analyzed using SEM.

■ ASSOCIATED CONTENT

Supporting Information

The Supporting Information is available free of charge at https://pubs.acs.org/doi/10.1021/acsomega.0c03053.

Coating deposition parameters; EDAX analysis of as-sprayed, FSP treated, and SFP treated Ni-Cr-5Al2O3 coating; SEM images of the top surfaces after potentiodynamic polarization testing; and XPS survey scan and atomic percentage of different elements in the oxide layer of the as-sprayed, FSP treated, and SFP treated Ni-Cr-5Al2O3 coating (PDF)

■ AUTHOR INFORMATION

Corresponding Author

Harpreet Singh Arora − *Surface Science and Tribology Lab, Department of Mechanical Engineering, Shiv Nadar University, Uttar Pradesh, Greater Noida 201314, India;* orcid.org/0000-0002-5674-2930; Email: harpreet.arora@snu.edu.in

Authors

Gopinath Perumal − *Surface Science and Tribology Lab, Department of Mechanical Engineering, Shiv Nadar University, Uttar Pradesh, Greater Noida 201314, India*

Manjeet Rani − *Surface Science and Tribology Lab, Department of Mechanical Engineering, Shiv Nadar University, Uttar Pradesh, Greater Noida 201314, India*

Harpreet S Grewal − *Surface Science and Tribology Lab, Department of Mechanical Engineering, Shiv Nadar University, Uttar Pradesh, Greater Noida 201314, India;* orcid.org/0000-0001-9265-4674

Complete contact information is available at: https://pubs.acs.org/10.1021/acsomega.0c03053

Author Contributions

#H.S.A. and G.P. contributed equally to this work.

Notes

The authors declare no competing financial interest.

■ ACKNOWLEDGMENTS

This research was supported by the project titled "Modulating Coating Properties for Enhanced Protection from Erosion−Corrosion: A Systematic Approach on Delineating the Effect of Post-Processing Conditions", Naval Research Board (NRB), project no.: NRB-399/MAT/17-18.

■ REFERENCES

(1) Wang, Y.; Tian, W.; Zhang, T.; Yang, Y. Microstructure, spallation and corrosion of plasma sprayed Al2O3−13%TiO2 coatings. *Corros. Sci.* **2009**, *51*, 2924−2931.

(2) Guo, R. Q.; Zhang, C.; Chen, Q.; Yang, Y.; Li, N.; Liu, L. Study of structure and corrosion resistance of Fe-based amorphous coatings prepared by HVAF and HVOF. *Corros. Sci.* **2011**, *53*, 2351−2356.

(3) Jiang, Q.; Miao, Q.; Liang, W.-P.; Ying, F.; Tong, F.; Xu, Y.; Ren, B.-L.; Yao, Z.-J.; Zhang, P.-Z. Corrosion behavior of arc sprayed Al−Zn−Si−RE coatings on mild steel in 3.5wt% NaCl solution. *Electrochim. Acta* **2014**, *115*, 644−656.

(4) da Silva, F. S.; Cinca, N.; Dosta, S.; Cano, I. G.; Couto, M.; Guilemany, J. M.; Benedetti, A. V. Corrosion behavior of WC-Co coatings deposited by cold gas spray onto AA 7075-T6. *Corros. Sci.* **2018**, *136*, 231−243.

(5) López-Ortega, A.; Arana, J. L.; Rodríguez, E.; Bayón, R. Corrosion, wear and tribocorrosion performance of a thermally sprayed aluminum coating modified by plasma electrolytic oxidation technique for offshore submerged components protection. *Corros. Sci.* **2018**, *143*, 258−280.

(6) Wu, J.; Zhang, S. D.; Sun, W. H.; Gao, Y.; Wang, J. Q. Enhanced corrosion resistance in Fe-based amorphous coatings through eliminating Cr-depleted zones. *Corros. Sci.* **2018**, *136*, 161−173.

(7) Matthews, S. J.; James, B. J.; Hyland, M. M. Microstructural influence on erosion behaviour of thermal spray coatings. *Mater. Charact.* **2007**, *58*, 59−64.

(8) Santa, J. F.; Espitia, L. A.; Blanco, J. A.; Romo, S. A.; Toro, A. Slurry and cavitation erosion resistance of thermal spray coatings. *Wear* **2009**, *267*, 160−167.

(9) Toma, D.; Brandl, W.; Marginean, G. Wear and corrosion behaviour of thermally sprayed cermet coatings. *Surf. Coat. Technol.* **2001**, *138*, 149−158.

(10) Huang, P.-K.; Yeh, J.-W.; Shun, T.-T.; Chen, S.-K. Multi-Principal-Element Alloys with Improved Oxidation and Wear Resistance for Thermal Spray Coating. *Adv. Eng. Mater.* **2004**, *6*, 74−78.

(11) Davis, J. R. *Handbook of Thermal Spray Technology*; ASM International, 2004.

(12) Sadeghi, E.; Markocsan, N.; Joshi, S. Advances in Corrosion-Resistant Thermal Spray Coatings for Renewable Energy Power Plants. Part I: Effect of Composition and Microstructure. *J. Therm. Spray Technol.* **2019**, *28*, 1749−1788.

(13) Knuuttila, J.; Sorsa, P.; Mäntylä, T.; Knuuttila, J.; Sorsa, P. Sealing of thermal spray coatings by impregnation. *J. Therm. Spray Technol.* **1999**, *8*, 249−257.

(14) Ctibor, P.; Neufuss, K.; Zahalka, F.; Kolman, B. Plasma sprayed ceramic coatings without and with epoxy resin sealing treatment and their wear resistance. *Wear* **2007**, *262*, 1274−1280.

(15) Liu, Z.; Yan, D.; Dong, Y.; Yang, Y.; Chu, Z.; Zhang, Z. The effect of modified epoxy sealing on the electrochemical corrosion behaviour of reactive plasma-sprayed TiN coatings. *Corros. Sci.* **2013**, *75*, 220−227.

(16) Kuang, X.; Zhou, Y.; Shi, Q.; Wang, T.; Qi, H. J. Recycling of Epoxy Thermoset and Composites via Good Solvent Assisted and Small Molecules Participated Exchange Reactions. *ACS Sustainable Chem. Eng.* **2018**, *6*, 9189−9197.

(17) Tian, F.; Wang, X.-L.; Yang, Y.; An, W.; Zhao, X.; Xu, S.; Wang, Y.-Z. Energy-Efficient Conversion of Amine-Cured Epoxy Resins into Functional Chemicals Based on Swelling-Induced Nanopores. *ACS Sustainable Chem. Eng.* **2020**, *8*, 2226−2235.

(18) Bergant, Z.; Trdan, U.; Grum, J. Effect of high-temperature furnace treatment on the microstructure and corrosion behavior of NiCrBSi flame-sprayed coatings. *Corros. Sci.* **2014**, *88*, 372−386.

(19) Gil, L.; Prato, M. A.; Staia, M. H. Effect of post-heat treatment on the corrosion resistance of NiWCrBSi HVOF coatings in chloride solution. *J. Therm. Spray Technol.* **2002**, *11*, 95−99.

(20) Li, W.-Y.; Li, C.-J.; Liao, H.; Coddet, C. Effect of heat treatment on the microstructure and microhardness of cold-sprayed tin bronze coating. *Appl. Surf. Sci.* **2007**, *253*, 5967−5971.

(21) Zhang, C.; Zhang, G.; Leparoux, S.; Liao, H.; Li, C.-X.; Li, C.-J.; Coddet, C. Microwave sintering of plasma-sprayed yttria stabilized zirconia electrolyte coating. *J. Eur. Ceram. Soc.* **2008**, *28*, 2529−2538.

(22) Janka, L.; Norpoth, J.; Eicher, S.; Rodríguez Ripoll, M.; Vuoristo, P. Improving the toughness of thermally sprayed Cr_3C_2-NiCr hardmetal coatings by laser post-treatment. *Mater. Des.* **2016**, *98*, 135−142.

(23) Yuanzheng, Y.; Youlan, Z.; Zhengyi, L.; Yuzhi, C. Laser remelting of plasma sprayed Al2O3 ceramic coatings and subsequent wear resistance. *Mater. Sci. Eng., A* **2000**, *291*, 168−172.

(24) González, R.; Cadenas, M.; Fernández, R.; Cortizo, J. L.; Rodríguez, E. Wear behaviour of flame sprayed NiCrBSi coating remelted by flame or by laser. *Wear* **2007**, *262*, 301−307.

(25) Shaw, L. L.; Goberman, D.; Ren, R.; Gell, M.; Jiang, S.; Wang, Y.; Xiao, T. D.; Strutt, P. R. The dependency of microstructure and

properties of nanostructured coatings on plasma spray conditions. *Surf. Coat. Technol.* **2000**, *130*, 1−8.
(26) Morisada, Y.; Fujii, H.; Mizuno, T.; Abe, G.; Nagaoka, T.; Fukusumi, M. Modification of thermally sprayed cemented carbide layer by friction stir processing. *Surf. Coat. Technol.* **2010**, *204*, 2459−2464.
(27) Hodder, K. J.; Izadi, H.; McDonald, A. G.; Gerlich, A. P. Fabrication of aluminum−alumina metal matrix composites via cold gas dynamic spraying at low pressure followed by friction stir processing. *Mater. Sci. Eng., A* **2012**, *556*, 114−121.
(28) Singh, S.; Gupta, D.; Jain, V.; Sharma, A. K. Microwave Processing of Materials and Applications in Manufacturing Industries: A Review. *Mater. Manuf. Processes* **2015**, *30*, 1−29.
(29) Voisey, K. T.; Liu, Z.; Stott, F. H. Inhibition of metal dusting using thermal spray coatings and laser treatment. *Surf. Coat. Technol.* **2006**, *201*, 637−648.
(30) Selvam, K.; Ayyagari, A.; Grewal, H. S.; Mukherjee, S.; Arora, H. S. Enhancing the erosion-corrosion resistance of steel through friction stir processing. *Wear* **2017**, *386-387*, 129−138.
(31) Selvam, K.; Mandal, P.; Grewal, H. S.; Arora, H. S. Ultrasonic cavitation erosion-corrosion behavior of friction stir processed stainless steel. *Ultrason. Sonochem.* **2018**, *44*, 331−339.
(32) Huang, C.; Li, W.; Zhang, Z.; Fu, M.; Planche, M.-P.; Liao, H.; Montavon, G. Modification of a cold sprayed SiCp/Al5056 composite coating by friction stir processing. *Surf. Coat. Technol.* **2016**, *296*, 69−75.
(33) Scherrer, P. Determination of the size and internal structure of colloidal particles using X-rays. *Nachr. Ges. Wiss. Göttingen.* **1918**, *2*, 98−100.
(34) Gubicza, J.; Chinh, N. Q.; Krállics, G.; Schiller, I.; Ungár, T. Microstructure of ultrafine-grained fcc metals produced by severe plastic deformation. *Curr. Appl. Phys.* **2006**, *6*, 194−199.
(35) Liscano, S.; Gil, L.; Staia, M. H. Effect of sealing treatment on the corrosion resistance of thermal-sprayed ceramic coatings. *Surf. Coat. Technol.* **2004**, *188-189*, 135−139.
(36) Liu, C.; Bi, Q.; Leyland, A.; Matthews, A. An electrochemical impedance spectroscopy study of the corrosion behaviour of PVD coated steels in 0.5 N NaCl aqueous solution: Part I. Establishment of equivalent circuits for EIS data modelling. *Corros. Sci.* **2003**, *45*, 1243−1256.
(37) Liu, C.; Bi, Q.; Leyland, A.; Matthews, A. An electrochemical impedance spectroscopy study of the corrosion behaviour of PVD coated steels in 0.5 N NaCl aqueous solution: Part II.: EIS interpretation of corrosion behaviour. *Corros. Sci.* **2003**, *45*, 1257−1273.
(38) Hlushko, H.; Cubides, Y.; Hlushko, R.; Kelly, T. M.; Castaneda, H.; Sukhishvili, S. A. Hydrophobic Antioxidant Polymers for Corrosion Protection of an Aluminum Alloy. *ACS Sustainable Chem. Eng.* **2018**, *6*, 14302−14313.
(39) McCafferty, E., *Introduction to Corrosion Science*. Springer New York : 2010, DOI: 10.1007/978-1-4419-0455-3.
(40) van Westing, E. P. M.; Ferrari, G. M.; de Wit, J. H. W. The determination of coating performance with impedance measurements—III. in situ determination of loss of adhesion. *Corros. Sci.* **1994**, *36*, 979−994.
(41) Mišković-stanković, V. B.; Dražić, D. M.; Teodorović, M. J. Electrolyte penetration through epoxy coatings electrodeposited on steel. *Corros. Sci.* **1995**, *37*, 241−252.

https://dx.doi.org/10.1021/acsomega.0c03053
ACS Omega 2020, 5, 24558−24566